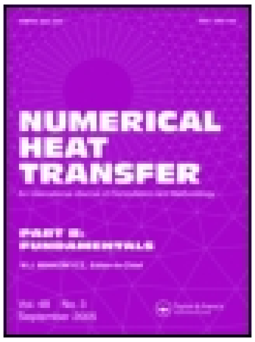

Numerical Heat Transfer, Part B: Fundamentals

ISSN: 1040-7790 (Print) 1521-0626 (Online) Journal homepage: http://www.tandfonline.com/loi/unhb20

A Compact Procedure for Discretization of the Anisotropic Diffusion Operator

M. Darwish & F. Moukalled

To cite this article: M. Darwish & F. Moukalled (2009) A Compact Procedure for Discretization of the Anisotropic Diffusion Operator, Numerical Heat Transfer, Part B: Fundamentals, 55:5, 339-360, DOI: 10.1080/10407790902816747

To link to this article: http://dx.doi.org/10.1080/10407790902816747

Numerical Heat Transfer, Part B, 55: 339–360, 2009

ISSN: 1040-7790 print/1521-0626 online
DOI: 10.1080/10407790902816747

A COMPACT PROCEDURE FOR DISCRETIZATION OF THE ANISOTROPIC DIFFUSION OPERATOR

M. Darwish and F. Moukalled
Department of Mechanical Engineering, American University of Beirut, Beirut, Lebanon

This article presents a conservative finite-volume-based scheme for discretization of the anisotropic diffusion operator, which is simple to implement and numerically conservative. The procedure is an extension of a standard method used for discretization of the isotropic diffusion operator in finite-volume methods. Consequently, the technique can be easily implemented in codes originally developed to solve isotropic diffusion problems. The method is applied in an unstructured finite-volume solver and assessed by solving the following four problems: (1) steady conduction in an anisotropic block, (2) anisotropic conduction with a source term, (3) anisotropic conduction in a hollow block, and (4) heterogeneous anisotropic conduction with embedded point heat sources. Calculations are performed for a wide range of parameters using triangular/quadrilateral cells on grid systems with sizes ranging between 10^2 and 3×10^5 control volumes, and convergence is accelerated through the use of an algebraic multigrid method. Converged solutions are obtained for all problems and on all grid systems used, and the results are in excellent agreement with the exact analytical solutions.

INTRODUCTION

Diffusion equations with anisotropic coefficients arise in many practical applications. Examples include contaminant transport in anisotropic media [1], solidification systems [2, 3], wave-front propagation in cardiac tissues [4], algorithms for de-noising images [5], and petroleum reservoirs, to cite a few. These physical situations are characterized by transport equations with a diffusion coefficient represented by a space-dependent full-rank tensor, which becomes diagonal if the reference system is aligned with the principal direction of anisotropy [6]. Moreover, the numerical solution to this class of problems requires careful consideration of the discretization procedure because it is highly dependent on the anisotropy ratio, i.e., the ratio between the smallest and largest eigenvalues of the diffusion tensor [7], values which can easily reach an order of 10^{-3}. As the value of the anisotropy ratio decreases, numerical instabilities arise, leading to error amplification that prohibits convergence, a phenomenon that is denoted in the literature as mesh locking

Received 4 April 2008; accepted 19 January 2009.

Financial support provided by the Lebanese National Council for Scientific Research through Grants 113040-022142 and 113040-022129 is gratefully acknowledged.

Address correspondence to F. Moukalled, Department of Mechanical Engineering, American University of Beirut, P.O. Box 11-0236, Riad El Solh, Beirut 1107 2020, Lebanon. E-mail: memouk@aub.edu.lb

NOMENCLATURE

a_P, a_F	coefficients in the discretized equation	Q	source term in the diffusion equation
b_P	source term in the discretized equation	$\mathbf{r}_{P\,\mathrm{or}\,F}$	distance vector to point P or F
d_{PF}	magnitude of $\mathbf{d}_{PF}$	$\mathbf{S}$	surface vector
$\mathbf{d}_{PF}$	distance vector between P and F	S_1, S_2	point heat sources
e	magnitude of $\mathbf{e}$	$\mathbf{T}$	distance vector equals $\mathbf{S}-\mathbf{E}$
$\mathbf{e}$	unit vector in the PF direction	ϕ	general scalar quantity
E	magnitude of $\mathbf{E}$	Ω	cell volume
$\mathbf{E}$	distance vector in the PF direction	**Subscripts**	
k	isotropic diffusion coefficient	f	refers to the interface
$k_{11}, \ldots$	components of the **K** tensor	F	refers to the F grid point
$\mathbf{K}$	diffusion tensor	nb	refers to the faces of a control volume
n	magnitude of $\mathbf{n}$	NB	refers to the neighbors of the main grid point
$\mathbf{n}$	unit vector normal to the control-volume surface	P	refers to the P grid point

[8–10]. To overcome these problems, a proper discretization of the tangential diffusion term that ensures conservation should be sought. Several finite-difference [11–15] and finite-volume [16–21] methods have been developed for discretizing the anisotropic part of the diffusion operator. A common feature of all these methods is their intricate discretization procedure, which complicates their implementation in general computational fluid dynamics (CFD) codes.

This article presents a conservative finite-volume-based scheme for discretizing the diffusion operator in the presence of high anisotropy, which is simple to implement and numerically conservative. Thus, the focus of the article is on the numerical solution of the anisotropic steady-state diffusion equation given by

$$-\nabla \cdot \mathbf{K}\nabla\phi = Q \quad \text{in } \Omega \quad \mathbf{K} = \begin{bmatrix} k_{11} & k_{12} \\ k_{21} & k_{22} \end{bmatrix} \tag{1}$$

where **K** is a 2×2 tensor field (a 3×3 in three dimensions) having the following characteristics (based on the thermodynamic principals and Onsager's reciprocity relation [22]),

$$k_{11} > 0 \qquad k_{22} > 0 \qquad k_{12} = k_{21} \qquad k_{11}k_{22} - k_{12}^2 > 0 \tag{2}$$

and Q is a source term or a forcing function.

In what follows, the standard discretization procedure for the isotropic diffusion operator is described briefly, followed by the newly suggested procedure for discretization of the anisotropic operator. The difference between the two discretization procedures is outlined. The new technique is implemented within an unstructured finite-volume framework and assessed by presenting solutions to four test problems over a wide range of parametric values and grid sizes.

ISOTROPIC DIFFUSION COEFFICIENT

Integrating the general diffusion equation over the control volume displayed in Figure 1*a* and transforming the volume integral of the diffusion term into a surface

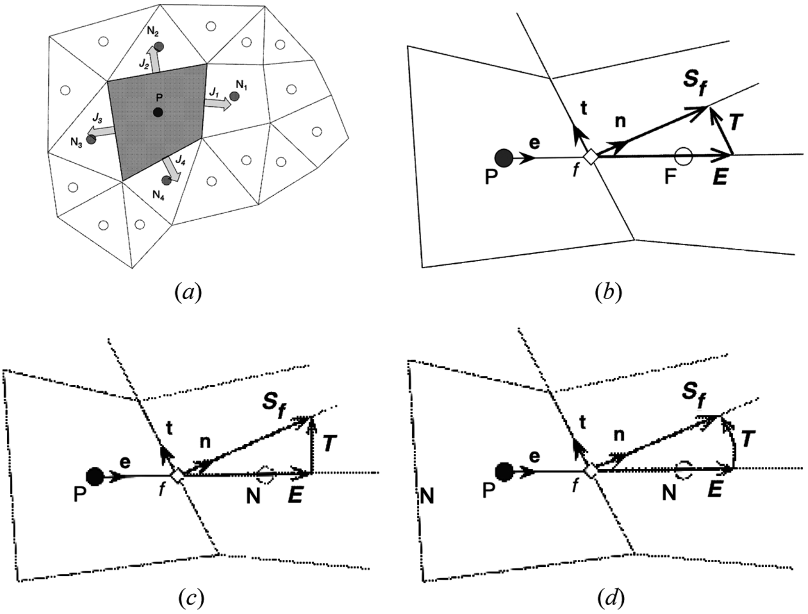

(*a*) (*b*)

(*c*) (*d*)

Figure 1. (*a*) Control volume; (*b–c*) decomposition of the surface vector into two components one aligned with the grid and one (*b*) normal to the surface vector, or (*c*) normal to the grid distance vector, or (*d*) decomposed such that the distance vector is of equal magnitude as the surface vector.

integral through the use of the Gauss divergence theorem, the semidiscretized form of Eq. (1) using the finite-volume method is given by

$$\int_{\partial\Omega_P} -(\mathbf{K}\nabla\phi)\cdot d\mathbf{S} = \int_{\Omega_P} Q\, d\Omega \tag{3}$$

For a polygonal surface the face integral can be written as

$$\sum_{f=\mathrm{nb}(\Omega_P)} \int_f -(\mathbf{K}\nabla\phi)\cdot d\mathbf{S} = \int_{\Omega_P} Q\, d\Omega \tag{4}$$

Using the midpoint integration rule for both the volume and surface integrals, Eq. (4) becomes

$$\sum_{f=\mathrm{nb}(\Omega_P)} (-\mathbf{K}\nabla\phi)_f \cdot \mathbf{S}_f = (Q\Omega)_P \tag{5}$$

for the case where the diffusivity is isotropic, **K** can be written as

$$\mathbf{K} = k\begin{bmatrix} 1 & 0 \\ 0 & 1 \end{bmatrix} \tag{6}$$

which, when substituted into the flux term, leads to

$$\mathbf{K}\nabla\phi = k\begin{bmatrix}1 & 0\\ 0 & 1\end{bmatrix}\begin{bmatrix}\frac{\partial\phi}{\partial x}\\ \frac{\partial\phi}{\partial y}\end{bmatrix} = k\nabla\phi \tag{7}$$

Thus Eq. (5) becomes

$$\sum_{f=\mathrm{nb}(\Omega_P)} k_f(-\nabla\phi\cdot\mathbf{S})_f = (Q\Omega)_P \tag{8}$$

The discretization of the term $(\nabla\phi\cdot\mathbf{S})_f$ in the finite-volume method follows a standard approach as outlined below.

The gradient along the direction normal to the surface is written as

$$\nabla\phi\cdot\mathbf{n} = \frac{\partial\phi}{\partial n} \tag{9}$$

which indicates that if the surface is not aligned with the cell centers, the gradient cannot be expressed as a function of the nodal ϕ values. Defining the **e** unit vector along the PF direction (Figure 1*b*) as

$$\mathbf{e} = \frac{\mathbf{r}_F - \mathbf{r}_P}{\|\mathbf{r}_F - \mathbf{r}_P\|} = \frac{\mathbf{d}_{PF}}{d_{PF}} \tag{10}$$

the gradient along the PF direction is given by

$$(\nabla\phi\cdot\mathbf{e})_f = \frac{\partial\phi}{\partial e} = \frac{\phi_F - \phi_P}{\|\mathbf{r}_F - \mathbf{r}_P\|} = \frac{\phi_F - \phi_P}{d_{PF}} \tag{11}$$

Thus, to linearize the flux on general nonorthogonal grids, the surface vector **S** is written as the sum of two vectors **E** and **T** ($\mathbf{S} = \mathbf{E} + \mathbf{T}$), with **E** directed along PF in order to discretize it as a function of the nodal values ϕ_F and ϕ_P. Introducing **E** and **T** (Figure 1*b*), the diffusion flux at *f* can be written as

$$\begin{aligned}\nabla\phi\cdot\mathbf{S} &= \underbrace{\nabla\phi\cdot\mathbf{E}}_{\substack{\text{orthogonal-like}\\ \text{contribution}}} + \underbrace{\nabla\phi\cdot\mathbf{T}}_{\substack{\text{non-orthogonal-like}\\ \text{contribution}}}\\ &= E\frac{\partial\phi}{\partial e} + \nabla\phi\cdot\mathbf{T} = E\frac{\phi_F - \phi_P}{d_{PF}} + \nabla\phi\cdot\mathbf{T}\end{aligned} \tag{12}$$

the first term on the right-hand side represents a contribution similar to that on orthogonal grids, i.e., involving ϕ_F and ϕ_P, while the second term on the right-hand side is called cross-diffusion or nonorthogonal diffusion and is due to the nonorthogonal nature of the grid. Several options can be used in defining **E** (Figures 1*b*–1*d*), which can be inferred from

$$\nabla\phi\cdot\mathbf{T} = \nabla\phi\cdot(\mathbf{S}-\mathbf{E}) = \begin{cases}\nabla\phi\cdot S(\mathbf{n} - \cos\theta\,\mathbf{e}) & \text{minimum correction}\\ \nabla\phi\cdot S(\mathbf{n} - \mathbf{e}) & \text{orthogonal correction}\\ \nabla\phi\cdot S\left(\mathbf{n} - \frac{1}{\cos\theta}\mathbf{e}\right) & \text{overrelaxed}\end{cases} \tag{13}$$

For orthogonal meshes, **n** and **e** are collinear, so θ is 0 and the cross-diffusion term is zero. Because the cross-diffusion term cannot be written as a function of the nodal values ϕ_F and ϕ_P, it is added as a source term in the control-volume algebraic equation. Substituting Eq. (12) into the semidiscretized equation yields

$$\begin{aligned}\sum_{f=\mathrm{nb}(P)}(-k\nabla\phi)_f\cdot\left(\mathbf{E}_f+\mathbf{T}_f\right)&=\sum_{f=\mathrm{nb}(P)}(-k\nabla\phi)_f\cdot\mathbf{E}_f+\sum_{f=\mathrm{nb}(P)}(-k\nabla\phi)_f\cdot\mathbf{T}_f\\&=\sum_{f=\mathrm{nb}(P)}\left(-k_fE_f\frac{\phi_F-\phi_P}{d_{PF}}\right)+\sum_{f=\mathrm{nb}(P)}(-k\nabla\phi)_f\cdot\mathbf{T}_f\end{aligned}\tag{14}$$

Upon expansion, the algebraic form obtained is

$$a_p\phi_p+\sum_{F=\mathrm{NB}(P)}a_F\phi_F=b_p\tag{15}$$

where

$$\begin{aligned}&a_F=-k_f\frac{E_f}{d_{PF}}\qquad a_P=-\sum_{F=\mathrm{NB}(P)}a_F\\&b_P=Q_P\Omega_P+\sum_{f=\mathrm{nb}(P)}(k\nabla\phi)_f\cdot\mathbf{T}_f\end{aligned}\tag{16}$$

The gradient appearing in b_P is calculated using values from the previous iteration, while $\mathbf{T}_f$ is a geometric quantity related to the surface vector decomposition method used.

ANISOTROPIC DIFFUSION COEFFICIENT

In the case where the diffusivity coefficient is a symmetric tensor, the diffusion equation becomes

$$\sum_{f=\mathrm{nb}(\Omega_P)}(-\mathbf{K}\nabla\phi)_f\cdot\mathbf{S}_f=(Q\Omega)_P\tag{17}$$

For this general case, the term $(-\mathbf{K}\nabla\phi)_f\cdot\mathbf{S}_f$ cannot be written as $-k(\nabla\phi\cdot\mathbf{S})_f$. Therefore the discretization procedure described in the previous section cannot be applied directly. However, through some manipulations, it will be shown that the procedure described above can be used.

In matrix form, the left-hand side of Eq. (17) can be written as

$$\begin{aligned}(-\mathbf{K}\nabla\phi)_f\cdot\mathbf{S}_f&=\sum_{f=\mathrm{nb}(\Omega_i)}\left\{-\begin{bmatrix}k_{11}&k_{12}\\k_{21}&k_{22}\end{bmatrix}_f\begin{bmatrix}\frac{\partial\phi}{\partial x}\\\frac{\partial\phi}{\partial y}\end{bmatrix}_f\right\}\cdot\mathbf{S}_f\\&=\sum_{f=\mathrm{nb}(\Omega_i)}-\begin{bmatrix}k_{11}\frac{\partial\phi}{\partial x}+k_{12}\frac{\partial\phi}{\partial y}\\k_{21}\frac{\partial\phi}{\partial x}+k_{22}\frac{\partial\phi}{\partial y}\end{bmatrix}_f\begin{bmatrix}S^x\\S^y\end{bmatrix}_f\\&=\sum_{f=\mathrm{nb}(\Omega_i)}-\begin{bmatrix}\frac{\partial\phi}{\partial x}&\frac{\partial\phi}{\partial y}\end{bmatrix}_f\begin{bmatrix}k_{11}&k_{21}\\k_{12}&k_{22}\end{bmatrix}_f\begin{bmatrix}S^x\\S^y\end{bmatrix}_f\\&=\sum_{f=\mathrm{nb}(\Omega_i)}-(\nabla\phi)_f\cdot\left(\mathbf{K}^T\mathbf{S}\right)_f=\sum_{f=\mathrm{nb}(\Omega_i)}-(\nabla\phi)_f\cdot\mathbf{S}'_f\end{aligned}\tag{18}$$

Substituting Eq. (18) into Eq. (17), the new form of the diffusion equation is given as

$$\sum_{f=\mathrm{nb}(\Omega_P)} (-\nabla\phi \cdot \mathbf{S}')_f = (Q\Omega)_P \tag{19}$$

In this form it is clear that the discretization procedure described above becomes applicable by simply setting k to 1 and replacing $\mathbf{S}$ with $\mathbf{S}' = \mathbf{K}^T\mathbf{S}$ ($\mathbf{K}^T$ is the transpose of $\mathbf{K}$). Therefore the codes originally developed for solving isotropic diffusion problems can be extended easily to handle anisotropic diffusion. Furthermore, extension to three-dimensional situations is straightforward.

RESULTS AND DISCUSSION

The performance of the newly developed discretization procedure is assessed in this section by presenting solutions to four anisotropic diffusion test problems on unstructured grids. The results are generated using triangular/quadrilateral control volumes on grid systems with mesh sizes ranging between 10^2 and 3×10^5 control volumes generated using a Delaunay triangulation mesher. Moreover, for all computations performed in this study, the algebraic systems of equations are solved using an algebraic multigrid technique [23] with an ILU(0) solver [24, 25] as a smoother and are underrelaxed using an underrelaxation factor value 0.9. The same initial guess was used for all grid sizes, and the computations were stopped when the maximum residual, defined as

$$\left\{\begin{array}{l} (\mathrm{RES})^{\phi} = \max\limits_{i=1}^{N} \dfrac{\left| a_P^{\phi}\phi_P + \sum_{F=\mathrm{NB}(P)} a_F^{\phi}\phi_F - b_P^{\phi} \right|}{a_P^{\phi}\phi_{\mathrm{scale}}} \\ \text{where} \\ \phi_{\mathrm{scale}} = \max\left(\phi_{P,\max} - \phi_{P,\min}, \phi_{P,\max}\right) \qquad \phi_{P,\max} = \max\limits_{i=1}^{N}(\phi_P) \qquad \phi_{P,\min} = \min\limits_{i=1}^{N}(\phi_P) \end{array}\right. \tag{20}$$

became smaller than the vanishing quantity ε, which was set at 10^{-5}.

Test 1: Steady Conduction in an Anisotropic Block

The physical situation, which represents a square cavity with a side of 1 m, is depicted in Figure 2. The orthotropic material used has a nonzero conductivity in the ξ direction ($k_{\xi\xi} \neq 0$) and a zero conductivity in the η direction ($k_{\eta\eta} = 0$). The solution is one-dimensional in the ξ direction (Figure 2) but fully two-dimensional in the (x, y) Cartesian coordinate system. If ξ is at an angle θ to the horizontal x axis, then the rotation matrix for a transformation from the (x, y) to the (η, ξ) coordinate system is given by

$$\mathbf{R}(\theta) = \begin{bmatrix} \cos\theta & \sin\theta \\ -\sin\theta & \cos\theta \end{bmatrix} \tag{21}$$

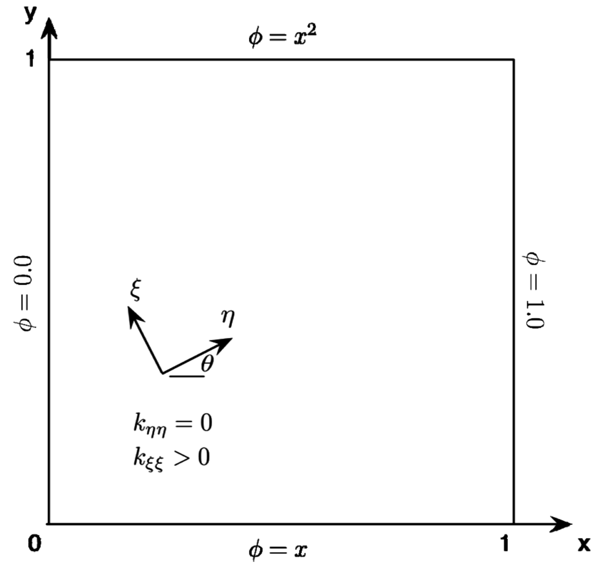

Figure 2. Physical domain for steady conduction in an anisotropic block problem.

and the transformation of the diffusion tensor can be written as

$$\mathbf{K}_{(\eta,\xi)} = \mathbf{R}(\theta)\mathbf{K}_{(x,y)}\mathbf{R}^T(\theta) \Rightarrow \mathbf{K}_{(x,y)} = \mathbf{R}^T(\theta)\mathbf{K}_{(\eta,\xi)}\mathbf{R}(\theta) \tag{22}$$

or, after manipulation, as

$$\begin{bmatrix} k_{xx} & k_{xy} \\ k_{yx} & k_{yy} \end{bmatrix} = \begin{bmatrix} k_{\eta\eta}\cos^2\theta + k_{\xi\xi}\sin^2\theta & \cos\theta\sin\theta(k_{\eta\eta} - k_{\xi\xi}) \\ \cos\theta\sin\theta(k_{\eta\eta} - k_{\xi\xi}) & k_{\eta\eta}\sin^2\theta + k_{\xi\xi}\cos^2\theta \end{bmatrix} \tag{23}$$

The problem is solved for $k_{\eta\eta} = 0$, $k_{\xi\xi} = 1$, and $\theta = \pi/6$ [10]. For the selected parametric values, the diffusion tensor is simplified to

$$\begin{bmatrix} k_{xx} & k_{xy} \\ k_{yx} & k_{yy} \end{bmatrix} = \begin{bmatrix} 1/4 & -\sqrt{3}/4 \\ -\sqrt{3}/4 & 3/4 \end{bmatrix} \tag{24}$$

Defining the angle α as the complementary of the angle θ ($\alpha = \pi/2 - \theta$), the exact analytical solution for the problem [10] is given by

$$\phi = \begin{cases} x & y + x\tan\alpha < 0 \\ \left[\frac{1-y}{1-y+(1-x)\tan\alpha}\right] & \\ *\left[1 + \frac{(1-x)\tan\alpha}{1-y}\left(x - \frac{1-y}{\tan\alpha}\right)^2\right] & y + x\tan\alpha - \tan\alpha > 0 \\ x + \frac{y}{\tan\alpha} + y\left[\left(x - \frac{1-y}{\tan\alpha}\right)^2 - \left(x + \frac{y}{\tan\alpha}\right)\right] & \text{elsewhere} \end{cases} \tag{25}$$

The results for the problem are presented in Figures 3 and 4. Figure 3 compares the exact solution with numerical solutions generated using grid networks with values of 10^2 (Figure 3*a*), 10^3 (Figure 3*b*), 10^4 (Figure 3*c*), 3×10^4 (Figure 3*d*), 5×10^4 (Figure 3*e*), 10^5 (Figure 3*f*), 2×10^5 (Figure 3*g*), and 3×10^5 (Figure 3*h*) control volumes. As depicted, the numerical solution is very close to the exact solution even for the coarsest grid presented (Figure 3*a*) and improves further as the grid density increases (Figures 3*b*–3*d*), falling on top of the exact solution on the densest grids

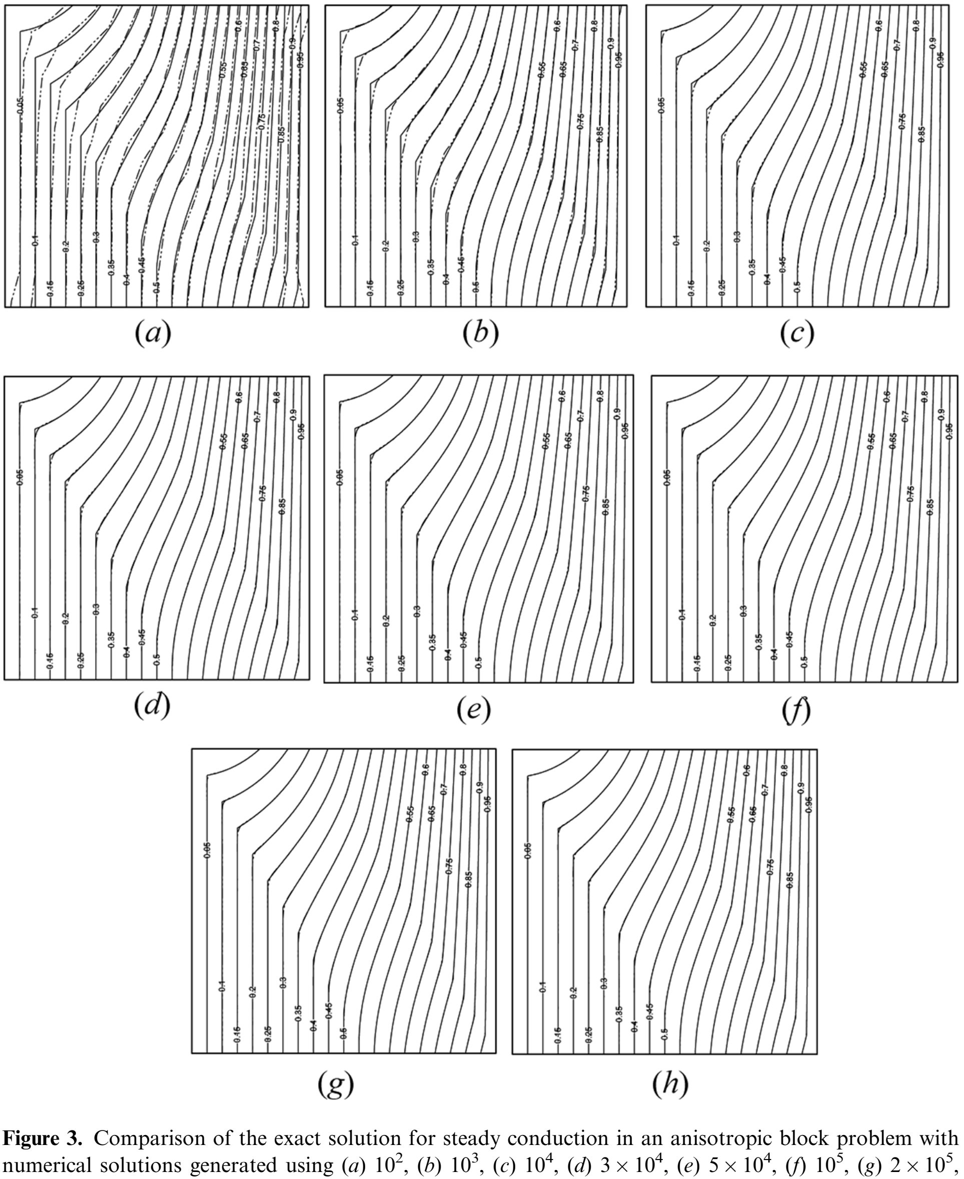

(*a*) (*b*) (*c*)

(*d*) (*e*) (*f*)

(*g*) (*h*)

Figure 3. Comparison of the exact solution for steady conduction in an anisotropic block problem with numerical solutions generated using (*a*) 10^2, (*b*) 10^3, (*c*) 10^4, (*d*) 3×10^4, (*e*) 5×10^4, (*f*) 10^5, (*g*) 2×10^5, and (*h*) 3×10^5 control volumes.

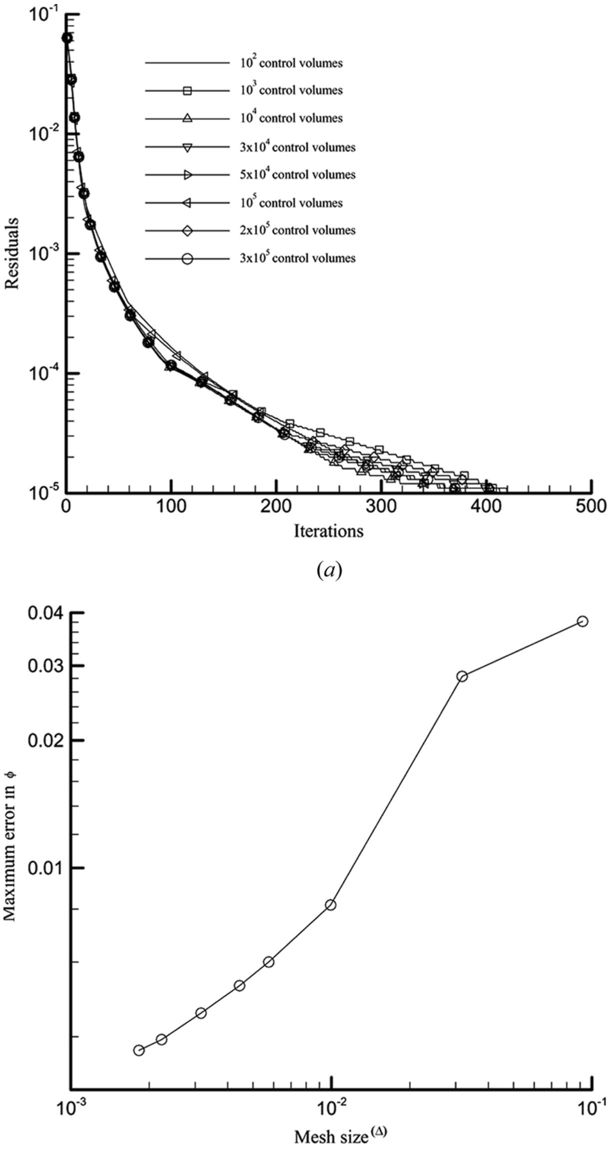

(*a*)

(*b*)

Figure 4. (*a*) Residual history plots on the various grids for the steady conduction in an anisotropic block problem, and (*b*) variation of the maximum solution error with grid size for steady conduction in an anisotropic block problem.

used (Figures 3*e*–3*h*). This is a clear demonstration of the correctness of the newly suggested discretization approach.

The convergence history plots, showing the decrease in the maximum residual with the iteration number for solutions obtained on the various grid systems, are displayed in Figure 4*a*. As shown, the number of iterations required for convergence to be reached is independent of the grid size, which is a characteristic of multigrid methods and an indication of the correct implementation of the algebraic multigrid solver.

The improvement in solution accuracy with grid refinement can be inferred from Figure 4*b*, which displays the variation of the maximum solution error with the mesh size Δ, defined as

$$\begin{cases} \text{Maximum error} = \max_{i=1}^{N} |\phi_{\text{exact}} - \phi_{\text{numerical}}| \\ \Delta = \sqrt{\frac{A}{N}} \end{cases} \tag{26}$$

where A is the area of the computational domain and N is the number of control volumes. As shown, the maximum error decreases almost linearly with a decrease in the mesh size. From Figure 3, it is obvious that this maximum error is located near the sharp discontinuity in slope.

Test 2: Anisotropic Conduction with a Source Term

The physical situation is depicted in Figure 5. The problem is chosen to evaluate the performance of the discretization procedure to the locking issue [26]. The governing conservation equation is written as

$$\nabla \cdot (\mathbf{K}\nabla\phi) = Q \qquad 0 < x < 0.5 \quad \text{and} \quad 0 < y < 0.5 \tag{27}$$

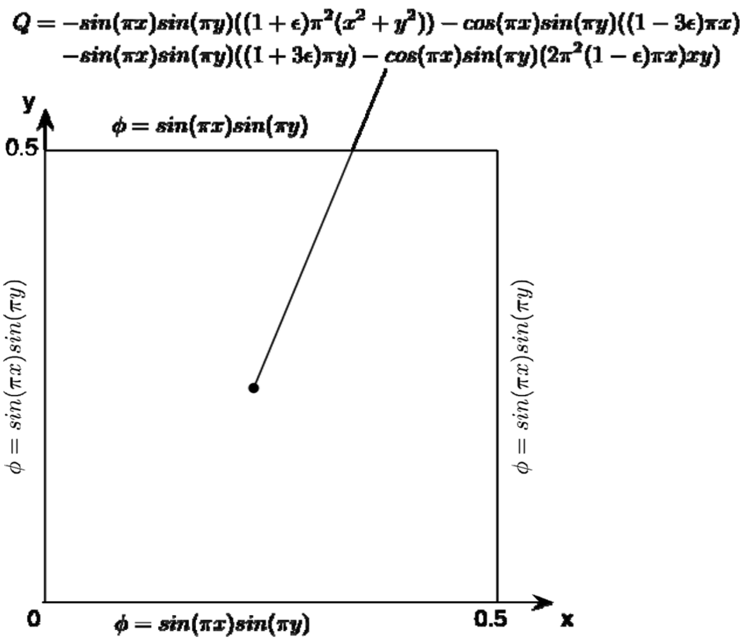

Figure 5. Physical domain for the anisotropic conduction with a source term problem.

where

$$\mathbf{K} = \begin{bmatrix} y^2 + \varepsilon x^2 & -(1-\varepsilon)xy \\ -(1-\varepsilon)xy & x^2 + \varepsilon y^2 \end{bmatrix} \tag{28}$$

The dirichlet boundary condition, used at all boundaries, and the source term Q are given by

$$\begin{aligned} \phi_{\text{boundary}} &= \sin(\pi x)\sin(\pi y) \\ Q &= -\sin(\pi x)\sin(\pi y)\left[(1+\varepsilon)\pi^2\left(x^2+y^2\right)\right] - \cos(\pi x)\sin(\pi y)[(1-3\varepsilon)\pi x] \\ &\quad - \sin(\pi x)\sin(\pi y)[(1+3\varepsilon)\pi x] - \cos(\pi x)\sin(\pi y)\left[2\pi^2(1-\varepsilon)\pi x\right]xy \end{aligned} \tag{29}$$

The parameter ε is assigned the values of 10^{-1}, 10^{-3}, 10^{-5}, and 10^{-7}. For each value, solutions are generated on the various grid sizes used. The anisotropic ratio for these cases varies between 10^{-1} and 10^{-7}. The exact analytical solution to this problem is independent of ε and is given by

$$\phi = \sin(\pi x)\sin(\pi y) \tag{30}$$

Comparisons of the numerical solution with the exact solution are presented in the form of ϕ-contour plots in Figures 6 and 7. The effect of grid refinement on the solution accuracy is shown in Figure 6, where numerical results generated on the various grid systems are compared with the analytical solution for $\varepsilon = 10^{-7}$. For this value of ε, the anisotropic ratio reaches a value as low as 10^{-7}. As in the previous test problem, results displayed in Figures 6*a*–6*h* show that the numerical solutions are very close to the exact solutions even on the coarsest mesh (Figure 6*a*), improve further with grid refinement (Figure 6*b*), and fall on top of the exact solutions for grid with sizes greater than 10^3 control volumes (Figures 6*c*–6*h*).

The numerical results presented in Figures 7*a*–7*d* are generated using a grid with a size of 10^4 control volumes but for different values of ε (the values of ε in Figures 7*a*, 7*b*, 7*c*, and 7*d* are 10^{-1}, 10^{-3}, 10^{-5}, and 10^{-7}, respectively). Even for this relatively coarse grid and for all values of ε, it is difficult to notice any difference between the numerical and exact solutions when both solutions are placed on top of each other to confirm, again, the correctness of the newly suggested discretization procedure.

The convergence history plots for all computed cases are displayed in Figure 8. In Figures 8*a*–8*d* convergence paths are presented for all grid sizes used at a given value of ε (the values of ε in Figures 8*a*, 8*b*, 8*c*, and 8*d* are 10^{-1}, 10^{-3}, 10^{-5}, and 10^{-7}, respectively). The required number of iterations for convergence to be reached is seen to be independent of the grid size for meshes greater than 10^3 control volumes, and independent of ε for ε greater than 10^{-1}. In all cases the convergence rate is reasonable, indicating the effectiveness of the discretization process.

The improvement in solution accuracy with grid refinement can be inferred from Figure 9, which displays the variation of the maximum solution error with the mesh size Δ, as defined in Eq. (26), for different values of ε. As shown, the highest accuracy is obtained for $\varepsilon = 10^{-1}$. For $\varepsilon > 10^{-1}$ the accuracy is nearly the same, with

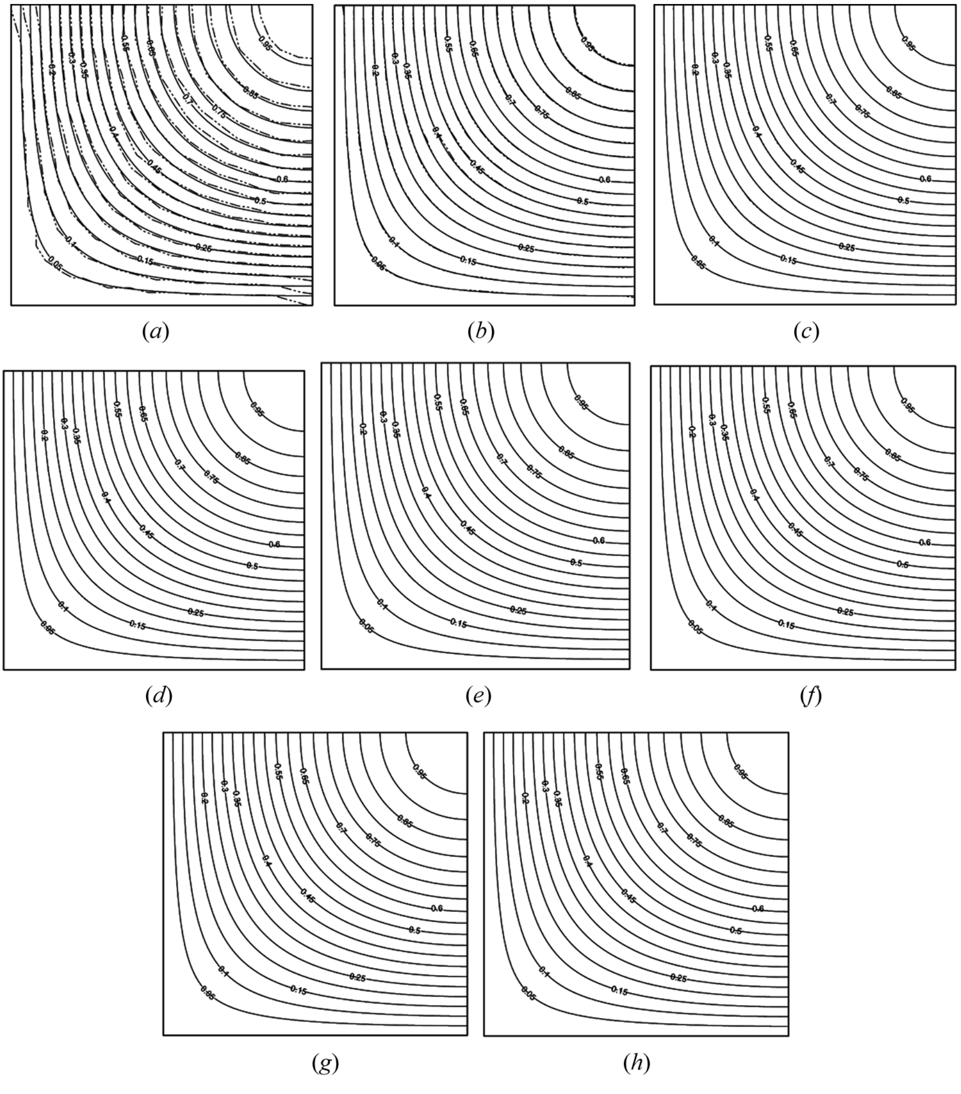

(*a*) (*b*) (*c*)

(*d*) (*e*) (*f*)

(*g*) (*h*)

Figure 6. Comparison of the exact solution for the anisotropic conduction with a source term problem with numerical solutions generated for $\varepsilon = 10^{-7}$ using (*a*) 10^2, (*b*) 10^3, (*c*) 10^4, (*d*) 3×10^4, (*e*) 5×10^4, (*f*) 10^5, (*g*) 2×10^5, and (*h*) 3×10^5 control volumes.

the maximum error for $\varepsilon = 10^{-3}$ being marginally less than the maximum errors for $\varepsilon = 10^{-5}$ and 10^{-7}. Also noted is the fact that the maximum error decreases almost linearly with a decrease in the mesh size until a value is reached below which the maximum error starts to slightly increase. This is attributed to the linear interpolation of the gradient, which may give rise to some unboundedness as will be described in the next problem.

For all results presented so far, uniform or nearly uniform grid systems were used. To check the performance of the newly developed scheme on a nonuniform

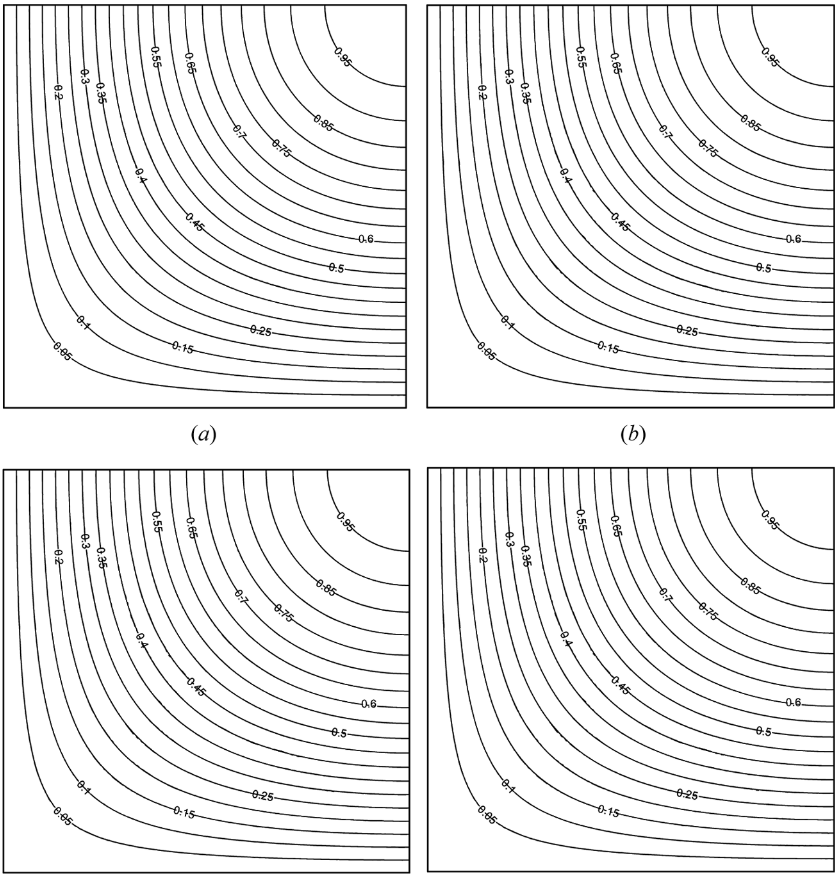

(*a*) (*b*)

(*c*) (*d*)

Figure 7. Comparison of the exact solution for the anisotropic conduction with a source term problem with numerical solutions generated using a grid size of 10^4 control volumes and for ε with a value of (*a*) 10^{-1}, (*b*) 10^{-3}, (*c*) 10^{-5}, and (*d*) 10^{-7}.

grid, the problem is solved using nonuniform quadrilateral and triangular grid systems of size 7×10^3 and 9×10^3 control volumes, respectively, and results are presented in Figure 10. Figures 10*a* and 10*c* display the nonuniform grid systems with quadrilateral and triangular elements, respectively, while Figures 10*b* and 10*d* show a comparison of the numerical solutions generated with the exact solution for the problem. As depicted, solutions generated are on top of the exact solution, verifying the capability of the new scheme to deal with anisotropic diffusion on general nonuniform grid systems.

Test 3: Anisotropic Conduction in a Hollow Block

The computational domain for the third test is shown in Figure 11. It represents a square with a side of 1 m with a square opening in the central portion with

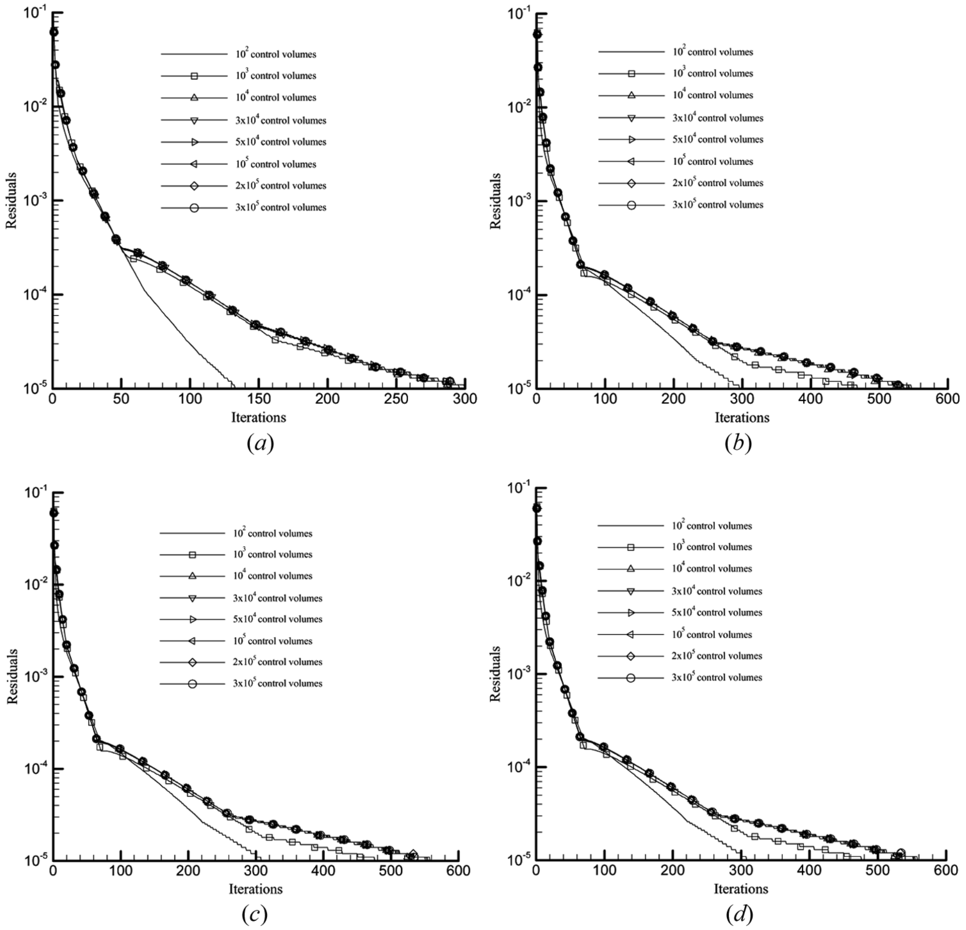

Figure 8. Residual history plots on the various grids for the anisotropic conduction with a source term problem for ε with a value of (*a*) 10^{-1}, (*b*) 10^{-3}, (*c*) 10^{-5}, and (*d*) 10^{-7}.

a side size of $1/15\,\text{m}$. The problem was studied in [27, 28] to assess the boundedness of the discretization procedure. The anisotropic conductivity matrix $\mathbf{K}$ is obtained by rotating the diagonal matrix through an angle $\theta = -\pi/3$ and is given by

$$\mathbf{K} = \begin{bmatrix} \frac{3}{4}\varepsilon + \frac{1}{4} & \frac{\sqrt{3}}{4}(\varepsilon - 1) \\ \frac{\sqrt{3}}{4}(\varepsilon - 1) & \frac{1}{4}\varepsilon \end{bmatrix} \tag{31}$$

Two anisotropic diffusivity ratios, $1/\varepsilon = 1/25$ and $1/100$, are used. A dirichlet condition of $\phi = 0$ is enforced on the outer boundaries, and $\phi = 2$ on the inner boundaries (Figure 11). Due to the unavailability of an exact analytical solution for the problem, the numerical solution obtained on the densest grid (3×10^5 control volumes) is used as the exact solution with which other numerical solutions are compared.

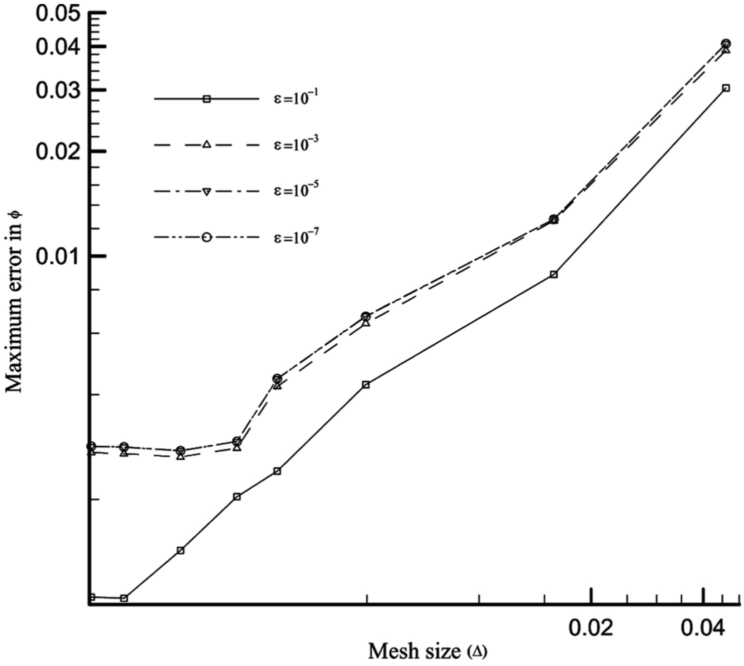

Figure 9. Variation of the maximum solution error with grid size for the anisotropic conduction with a source term problem.

The results for the problem are presented in Figures 12–14. Figures 12 and 13 compare the exact solution with numerical solutions generated using grid networks with sizes of 10^2 (Figures 12*a* and 13*a*), 10^3 (Figures 12*b* and 13*b*), 10^4 (Figures 12*c* and 13*c*), 5×10^4 (Figures 12*d* and 13*d*), 10^5 (Figures 12*e* and 13*e*), and 2×10^5 (Figures 12*f* and 13*f*) control volumes. Figure 12 presents results for an anisotropic diffusivity ratio of 1/25, while Figure 13 displays similar results for an anisotropic diffusivity ratio with a value of 1/100. The numerical solutions are seen to be close to the exact solution even on the coarsest grid presented (Figures 12*a* and 13*a*) and improves further as the grid density increases.

The convergence history plots showing the decrease in the maximum residual with the iteration number for solutions obtained on the various grid systems are displayed in Figure 14*a* for an anisotropic diffusivity ratio of 1/25 and in Figure 14*b* for a ratio of 1/100. The required number of iterations is higher than in the previous two problems and increases with increase to the anisotropic diffusivity ratio. Even in these situations, convergence was obtained on all grid sizes.

In the absence of any source term, the solution is bounded by the minimum and maximum values at the boundaries. Therefore, the solution should be between 0 and 2. The numerical solutions obtained are found to be bounded from above by 2. On the other hand, values below 0 are obtained on all grid systems, and the maximum unboundedness is presented in Table 1 as a function of the mesh size Δ

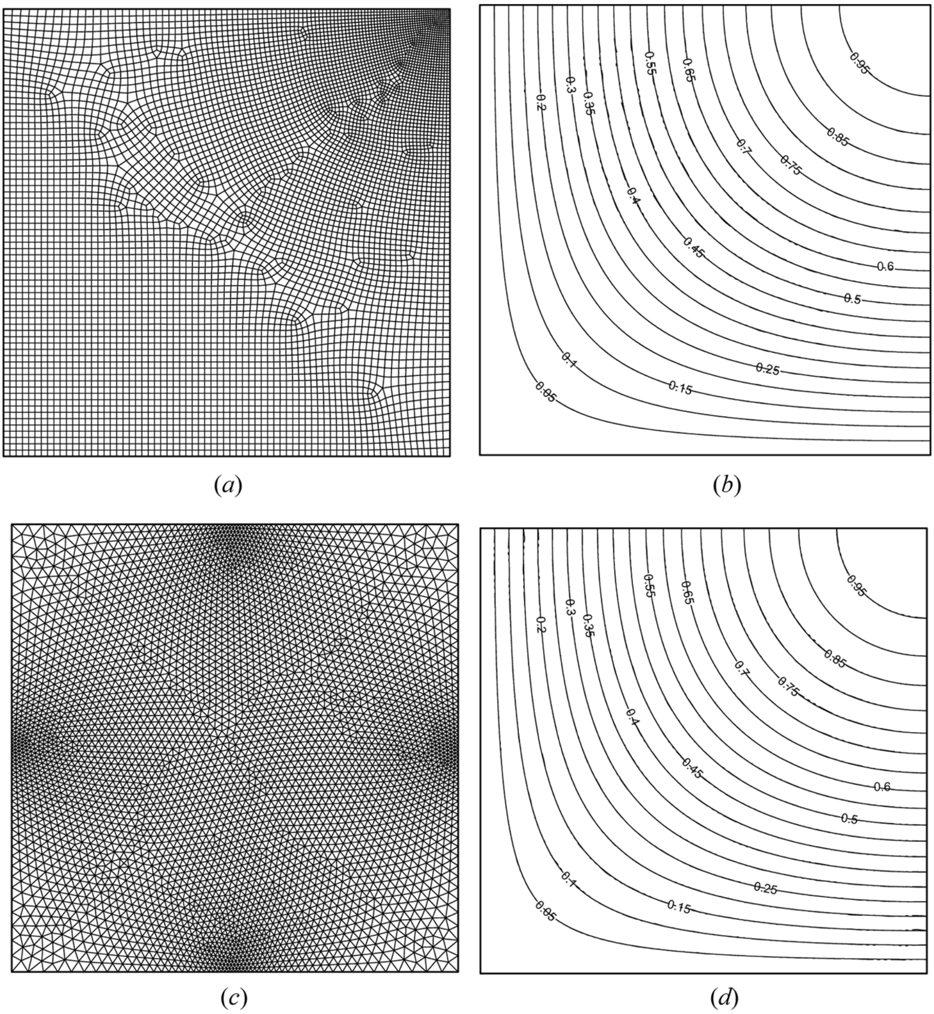

Figure 10. Comparison of the exact solution for the anisotropic conduction with a source term problem with numerical solutions generated using a nonuniform rectangular grid with a size of 7×10^3 control volumes (*a, b*), and a nonuniform triangular grid with a size of 9×10^3 control volumes (*c, d*), for $\varepsilon = 10^{-7}$.

[Eq. (26)] for both anisotropic ratios ($\varepsilon = 1/25$ and $\varepsilon = 1/100$). Except on the coarsest grid (10^2 cells), the unboundedness is of the order of 10^{-5}, which is close to zero. This unboundedness is a characteristic of linear diffusion formulations, has been reported by many researchers (e.g., [28, 29]), and is the result of violating the discrete maximum principle, which is the discrete analog of the maximum principle. In a recent article, Liska and Shashkov [28] reported on a method that preserves the solution boundedness by enforcing the discrete maximum principle using nonlinear gradient interpolation. Because the intention here is to present a compact discretization procedure for anisotropic diffusion, addressing this issue is beyond the scope of the current work and will be addressed in future research.

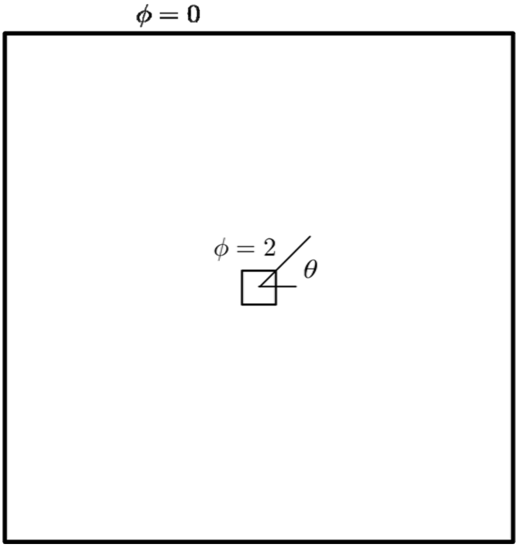

Figure 11. Physical domain for the anisotropic conduction in a hollow block problem.

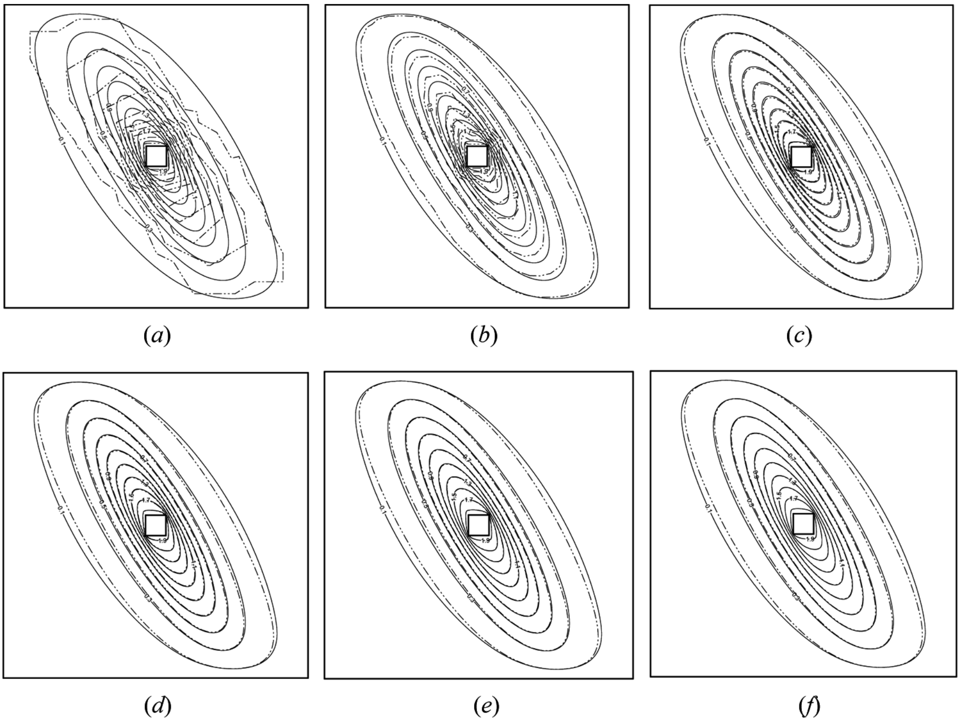
(*a*) (*b*) (*c*)

(*d*) (*e*) (*f*)

Figure 12. Comparison of the densest grid solution (3×10^5 cells) for the anisotropic conduction in a hollow block problem with numerical solutions for an anisotropic diffusivity ratio of $1/25$ generated using a grid size of (*a*) 10^2, (*b*) 10^3, (*c*) 10^4, (*d*) 5×10^4, (*e*) 10^5, and (*f*) 2×10^5 cells.

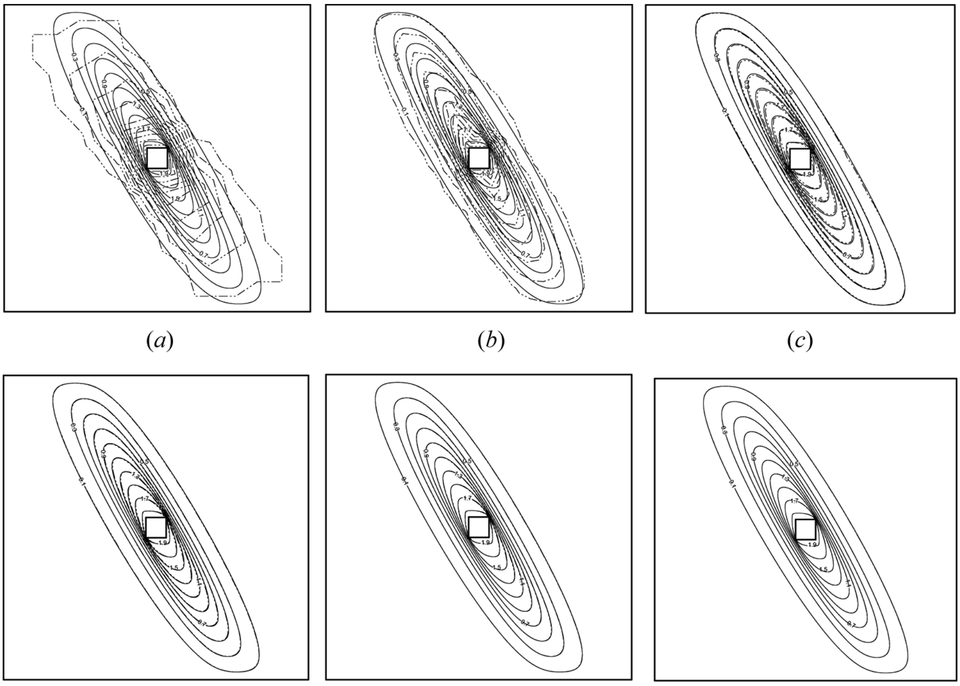

(*a*) (*b*) (*c*)

(*d*) (*e*) (*f*)

Figure 13. Comparison of the densest grid solution (3×10^5 cells) for the anisotropic conduction in a hollow block problem with numerical solutions for an anisotropic diffusivity ratio of $1/100$ generated using a grid size of (*a*) 10^2, (*b*) 10^3, (*c*) 10^4, (*d*) 5×10^4, (*e*) 10^5, and (*f*) 2×10^5 cells.

Test 4: Heterogeneous Anisotropic Conduction with Embedded Point Heat Sources

The computational domain for the fourth test is shown in Figure 15*a*. It represents a square block with a side of 10 m within which a core column of dissimilar material and of circular cross section (4 m in diameter) is embedded [30]. The problem is solved for the case when the lower and upper horizontal walls of the square block are maintained at 273 and 373 K, respectively, while the vertical walls are insulated. In addition, five discrete point heat sources of different strength ($S_1 = 2{,}000$ w and $S_2 = 1{,}000$ w) are distributed over the domain as shown in Figure 15*a*. The thermal diffusion coefficient tensors of the square block ($\mathbf{K}_b$) and core column ($\mathbf{K}_c$) are given by

$$\mathbf{K}_b = \begin{bmatrix} 7.7 & -2.0785 \\ -2.0785 & 10.1 \end{bmatrix} \quad \mathbf{K}_c = \begin{bmatrix} 24.15 & 1.05 \\ 1.05 & 24.15 \end{bmatrix} \tag{32}$$

The grid used in solving the problem is depicted in Figure 15*b* and is composed of around 10^4 control volumes. The ability of the proposed scheme to handle heterogeneous anisotropic situations is demonstrated in this problem by comparing

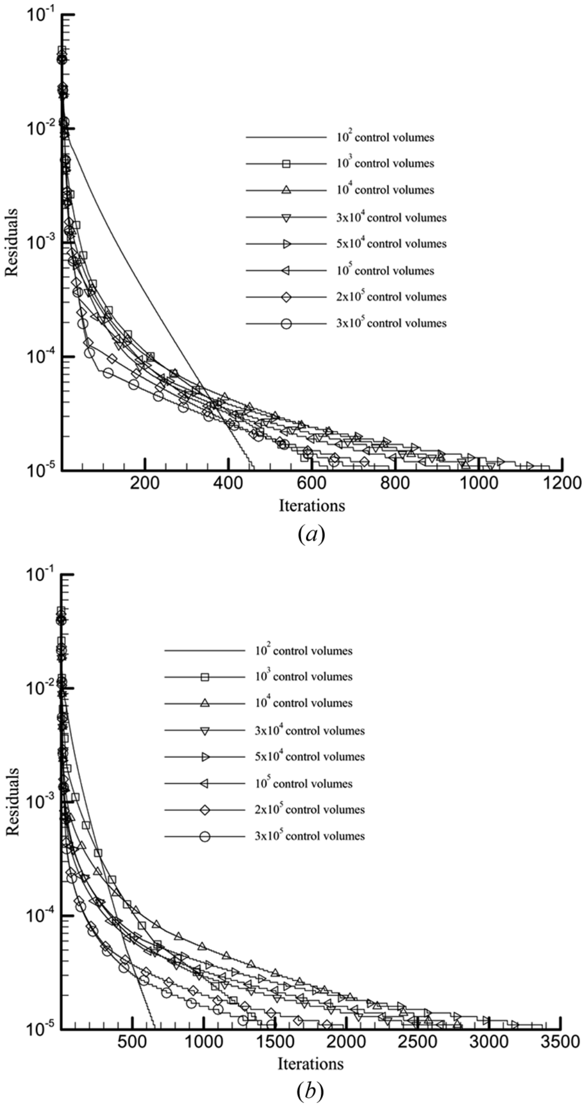

Figure 14. Residual history plots on the various grids for the anisotropic conduction in a hollow block problem for an anisotropic diffusivity ratio of (*a*) 1/25, and (*b*) 1/100.

generated results with similar ones obtained using commercial software, and results are displayed in Figures 15*c* and 15*d*. Figure 15*c* compares the computed temperatures along the left and right insulated walls of the square block, while Figure 15*d* compares temperature values around the circumference of the core column (i.e., the interface between the two dissimilar materials). As shown, profiles generated using the suggested scheme and those obtained using the commercial code are in excellent agreement and fall almost on top of each other, confirming once more the correctness of the developed scheme.

Table 1. Maximum unboundedness in the solution of the anisotropic conduction in a hollow block problem

	Δ							
ε	9.97e-2	3.15e-2	9.97e-3	5.76e-3	4.46e-3	3.15e-3	2.23e-3	1.82e-3
1/25	−0.055	−1.7e-5	−1.5e-5	−2.4e-5	−1e-6	−5.7e-5	−7.9e-5	−8.9e-5
1/100	−0.217	−6.3e-3	−1.1e-5	−3.2e-5	−2.3e-5	−3.5e-5	−5e-5	−8e-5

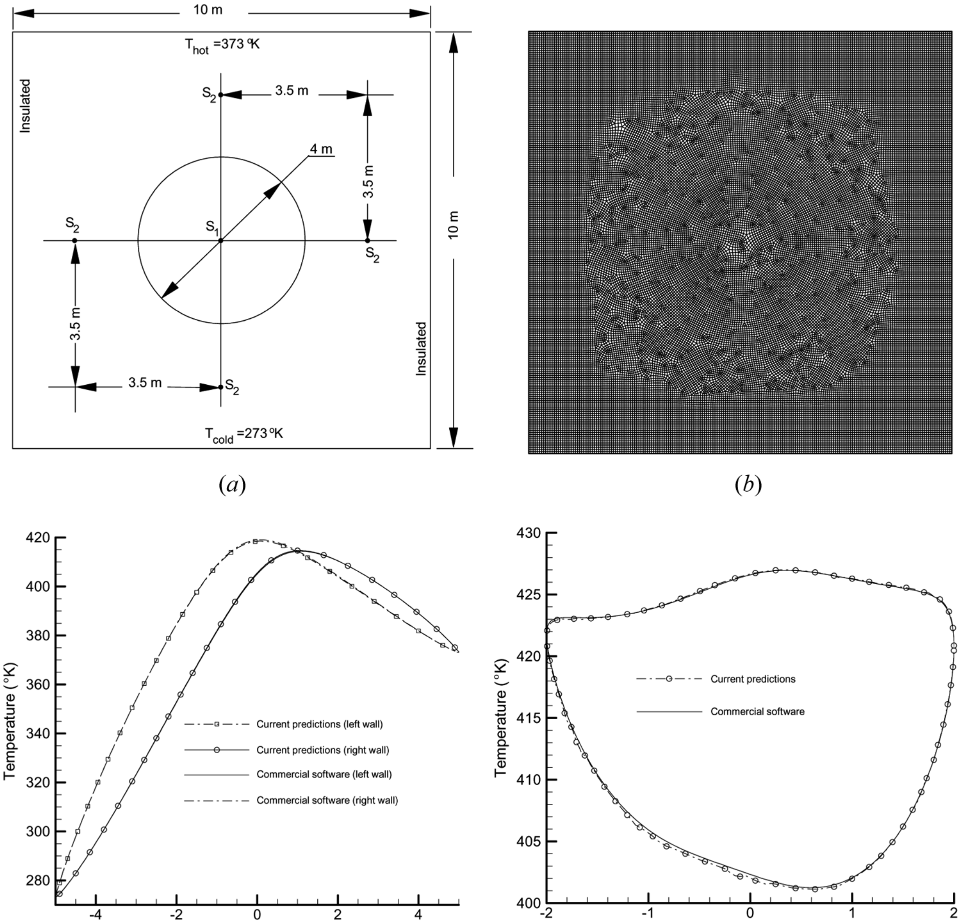

(*a*) (*b*)

(*c*) (*d*)

Figure 15. Physical domain (*a*) and grid system used (*b*); comparison of temperature variation along insulated left and right walls (*c*) and along the circumference of the core material (*d*) generated using the new discretization method and a commercial software for the anisotropic conduction in a square block with a core column problem.

CLOSING REMARKS

A conservative finite-volume-based scheme for the discretization of the anisotropic diffusion operator was presented. The procedure, which was shown to be an extension of a standard method used for discretization of the isotropic diffusion operator, is easy to implement in codes originally developed to solve isotropic diffusion problems. The method was implemented in an unstructured finite-volume solver and was assessed by solving four test problems over a wide range of parameters using triangular and quadrilateral cells on grid systems with mesh sizes ranging between 10^2 and 3×10^5 control volumes. The results computed were found to be in excellent agreement with available analytical solutions or available numerical predictions.

REFERENCES

1. P. Knabner, J. W. Barrett, and H. Kappmeier, Lagrange-Galerkin Approximation for Advection-Dominated Nonlinear Contaminant Transport in Porous Media, in A. Peters et al. (eds.), *Computational Methods in Water Resources X*, vol. 1, pp. 299–308, Kluwer Academic, Dordrecht, The Netherlands, 1994.
2. S. K. Sinha, T. Sundararajan, and V. K. Gard, A Variable Property Analysis of Alloy Solidification Using the Anisotropic Porous Medium Approach, *Int. J. Heat Mass Transfer*, vol. 35, pp. 2865–2877, 1992.
3. J. A. Weaver and R. Viskanta, Effects of Anisotropic Heat Conduction on Solidification, *Numer. Heat Transfer A*, vol. 15, pp. 181–195, 1989.
4. V. Jacquement and C. S. Henriquez, Finite Volume Stiffness Matrix for Solving Anisotropic Cardiac Propagation in 2D and 3D Unstructured Meshes, *IEEE Trans. Biomed. Eng.*, vol. 52, pp. 1490–1492, 2005.
5. S. K. Weeratunga and C. Kamath, PDE-Based Non-linear Anisotropic Diffusion Techniques for Denoising Scientific/Industrial Images: An Empirical Study, *Proc. Image Processing: Algorithms and Systems*, SPIE Electronic Imaging, San Jose, CA, 2002, pp. 279–290.
6. J. Bear, *Dynamics of Fluids in Porous Media*, Dover, New York, 1972.
7. I. Babuska and M. Suri, On Locking and Robustness in the Finite Element Method, *SIAM J. Numer. Anal.*, vol. 29, pp. 1261–1293, 1992.
8. G. Manzini and M. Putti, Mesh Locking Effects in the Finite Volume Solution of 2-D Anisotropic Diffusion Equations, *J. Comput. Phys.*, vol. 220, pp. 751–771, 2007.
9. V. Havu, An Analysis of Asymptotic Consistency Error in a Parameter Dependent Model Problem, *Calcolo*, vol. 40, no. 2, pp. 121–130, 2003.
10. V. Havu and J. Pitkäranta, An Analysis of Finite Element Locking in a Parameter Dependent Model Problem, *Numer. Math.*, vol. 89, pp. 691–714, 2001.
11. G. E. Forsythe and W. R. Easow, *Finite Different Method for the Partial Differential Equations*, Wiley, New York, 1960.
12. H. A. Friedman and B. L. McFarland, Two-Dimensional Ablation and Heat Conduction Analysis for Multimaterial Thrust Chamber Wall, *J. Spacecraft Rockets*, vol. 5, pp. 753–761, 1968.
13. D. J. Rose, H. Shao, and C. S. Henriquez, Discretization of Anisotropic Convection-Diffusion Equations, Convective M-Matrices and Their Iterative Solution, *VLSI Design*, vol. 10, pp. 485–529, 2000.
14. M. Krzek and L. Liu, Finite Element Approximation of a Nonlinear Heat Conduction Problem in Anisotropic Media, *Comput. Meth. Appl. Mech. Eng.*, vol. 157, pp. 387–397, 1998.

15. P. A. Jayantha and I. W. Turner, A Second Order Control-Volume Finite-Element Least-Squares Strategy for Simulating Diffusion in Anisotropic Media, *J. Comput. Math.*, vol. 23, pp. 1–16, 2005.
16. B. F. Balckwell and R. E. Hogan, Numerical Solution of Axisymmetric Heat Conduction Problems Using the Finite Control Volume Technique, *J. Thermophys. Heat Transfer*, vol. 7, pp. 462–471, 1993.
17. S. Wang, Solving Convection-Dominated Anisotropic Diffusion Equations by an Exponentially Fitted Finite Volume Method, *Comput. Math. Appl.*, vol. 44, pp. 1249–1265, 2002.
18. P. A. Jayantha and I. W. Turner, On the Use of Surface Interpolation Techniques in Generalised Finite Volume Strategies for Simulating Transport in Highly Anisotropic Porous Media, *J. Comput. Appl. Math.*, vol. 152, pp. 199–216, 2003.
19. E. Bertolazzi and G. Manzini, A Second-Order Maximum Principle Preserving Finite Volume Method for Steady Convection–Diffusion Problems, *SIAM J. Numer. Anal.*, vol. 43, pp. 2172–2199, 2006.
20. K. Domelevo and P. Omnes, A Finite Volume Method for the Laplace Equation on Almost Arbitrary Two-Dimensional Grids, *Math. Modell. Numer. Anal.*, vol. 39, pp. 1203–1249, 2005.
21. E. Eymard, T. Gallouêt, and R. Herbin, A Finite Volume Scheme for Anisotropic Diffusion Problem, *C. R. Math.*, vol. 339, pp. 299–302, 2004.
22. L. Onsager, Reciprocal Relations in Irreversible Processes I, *Phys. Rev.*, vol. 37, pp. 405–426, 1931.
23. B. R. Hutchinson and G. D. Raithby, A Multigrid Method Based on the Additive Correction Strategy, *Numer. Heat Transfer*, vol. 9, pp. 511–537, 1986.
24. C. Pommerell, Solution of Large Unsymmetric Systems of Linear Equations, *Ser. Microelectronics*, vol. 17, pp. 1–183, 1992.
25. C. Pommerell and W. Fichtner, Memory Aspects and Performance of Iterative Solvers, *SIAM J. Sci. Stat. Comput.*, vol. 15, pp. 460–473, 1994.
26. C. Le Potier, Finite Volume Scheme for Highly Anisotropic Diffusion Operators on Unstructured Meshes, *C. R. Math.*, vol. 340, pp. 921–926, 2005.
27. M. Mlacnik, L. Durlofsky, R. Juanes, and H. Tchelepi, Multipoint Flux Approximations for Reservoir simulation, *12th Annual SUPRI-HW Meeting*, Stanford University, Nov. 18–19, 2004.
28. R. Liska and M. Shashkov, Enforcing the Discrete Maximum Principle for Linear Finite Element Solutions of Second-Order Elliptic Problems, *Commun. Comput. Phys.*, vol. 3, pp. 852–877, 2008.
29. A. Draganescu, T. F. Dupont, and L. R. Scott, Failure of the Discrete Maximum Principle for an Elliptic Finite Element Problem, *Math. Comput.*, vol. 74, pp. 1–23, 2005.
30. Y. C. Shiah, P.-W. Hwang, and R.-B. Yang, Heat Conduction in Multiply Adjoined Anisotropic Media with Embedded Point Heat Sources, *J. Heat Transfer*, vol. 128, pp. 207–214, 2006.